This is the final peer-reviewed accepted manuscript of:

Fernando Claudio Spengler, Rejane De Césaro Oliveski, Luiz Alberto Oliveira Rocha, Cesare Biserni

Effect of extended surfaces on lauric acid melting process in annular cavities

In *Journal of Energy Storage, Volume 46, 2022*

The final published version is available online at:

https://doi.org/10.1016/j.est.2021.103867

Rights / License:

The terms and conditions for the reuse of this version of the manuscript are specified in the publishing policy. For all terms of use and more information see the publisher's website.

This item was downloaded from IRIS Università di Bologna (https://cris.unibo.it/)

When citing, please refer to the published version.

NUMERICAL INVESTIGATION ON LURIC ACID MELTING PROCESS IN HEAT EXCHANGERS: EFFECT OF THE FIN GEOMETRIC PARAMETERS

Fernando Claudio Spengler[1], Rejane De Césaro Oliveski[1], Luiz Alberto Oliveira Rocha[1], and Cesare Biserni[2]

[1]Mechanical Engineering Graduate Program, Universidade do Vale do Rio dos Sinos, 93022-750 São Leopoldo, Brazil

[2] Department of Industrial Engineering, Alma Mater Studiorum, University of Bologna, Viale Risorgimento 2, 40136 Bologna, Italy.

Abstract*. Thermal energy storage makes it possible to adjust energy availability and demand. Systems that use latent heat storage (LHTES) have high energy density and low thermal variation during the charge and discharge cycles. The phase change materials (PCM) used in these systems generally have low thermal conductivity, which makes the energy charge and discharge cycles prolonged. To enhance the heat exchange in these systems, several approaches have been presented in the literature. Among these different solutions, the use of extended surfaces has shown good results. The effect related to the variation of the fins geometric proportions on the PCM melting process is still a gap, and the present work aims to analyze the effect of the fins positioning and aspect ratio variation, in an annular cavity, filled with lauric acid. In total, 46 geometric configurations of the fin were studied, keeping constant its transversal area (length x thickness), but varying between 5 aspect ratios (length / thickness), for 5 different area ratios (fin area / cavity area). The study was performed by numerical simulation with the finite volume method. The numerical model is composed of the continuity, momentum conservation, and energy conservation equations, plus the enthalpy-porosity phase change model. It was validated with the experimental results of the literature. The computational mesh was evaluated using the Grid Convergence Index (GCI), resulting in an average index of 0.003%. For the analysis of the results, the melting time was considered as a performance indicator. The different heat exchange behaviors throughout the phase change process are analyzed in terms of liquid fraction vs Fourrier and Nusselt number vs. Fourier. The melting enhancement of the studied cases is also analyzed. This set of results showed that: the total melting time in systems with vertical fin arrangements is approximately 44% less than in systems with horizontal fin arrangements; the melting rate in systems with horizontal fin arrangements is 15% higher than systems with vertical fins, while*

there is solid PCM in the upper region of the cavity; for systems with area ratio ϕ = 0.003, the increase in the fin aspect ratio entails in a total melting time reduction higher than 11% in vertical fins arrangements, and lower than 2% in horizontal fins arrangements.

Keywords: *CFD. PCM. Lauric Acid. Melting. Fins.*

Nomenclature

A	area	[m^2]
a	fin width	[m]
b	fin length	[m]
C	mushy zone constant	[kg m^{-3} s^{-1}]
c_p	specific heat	[J kg^{-1} K^{-1}]
D	diameter	[m]
dt	time step	[s]
e	error	[-]
Fo	Fourier number	[-]
g	gravity acceleration	[m s^{-2}]
GCI	grid convergence index	[-]
h	heat transfer coefficient	[W m^{-2} K^{-1}]
hr	representative mesh size	[-]
k	thermal conductivity	[W m^{-1} K^{-1}]
L	latent heat	[J kg^{-1}]
Lc	characteristic length	[m]
m	mass	[kg]
N	number of elements	[-]
Nu	Nusselt number	[-]
p	pressure	[Pa]
$\dot{Q}$	heat transfer rate	[W]
q"	heat flow	[W m^{-2}]
R	radius	[m]
AR	aspect ratio	[-]
$\vec{S}$	source term	[Pa m^{-1}; W m^{-3}]
T	temperature	[K]

58	t	time	[s]
59	$\vec{V}$	velocity vector	[m s^{-1}]

60 ***Greek Symbols***

61	α	thermal diffusivity	[m^2 s^{-1}]
62	β	liquid fraction	[-]
63	γ	volume fraction	[-]
64	Δ	variation	[-]
65	ε	numeric constant	[-]
66	ζ	thermal expansion coefficient	[K^{-1}]
67	η_f	fin efficiency	[-]
68	λ	specific enthalpy	[J kg^{-1}]
69	μ	dynamic viscosity	[kg m^{-1} s^{-1}]
70	υ	kinematic viscosity	[m^2 s^{-1}]
71	ρ	density	[kg m^{-3}]
72	ϕ	fraction of fin area in cavity	[-]

73 ***Subscripts***

74	*0*	without fins
75	*cr*	*critical*
76	*ext*	external
77	f	fin
78	*i*	element
79	*int*	internal
80	*l*	liquid
81	*m*	melting
82	*min*	minimum
83	*s*	solid
84	se	section
85	*w*	wall

1 Introduction

Phase change materials (PCM) systems for heating and cooling solutions are used in a variety of areas such as building construction; vehicle thermal comfort; medical, pharmaceutical and chemical transport solutions; electronic cooling; solar water heating systems, the textile industry [1]. These latent heat storage systems (LHTES) have high energy storage density resulting in a more compact energy storage system [2]. Moreover, they benefit from constant temperature (for pure substances) during energy charge and discharge [3].

Thermal comfort solutions normally require a temperature range between 0 and 60 °C. This temperature range is compatible with the phase change (solid-liquid) of organic PCM. Which are and widely available in nature, besides being non-toxic, non-corrosive, and chemically stable. However, most PCM has low thermal conductivity. This fact eventually requires techniques for increasing heat transfer to optimize energy loading and unloading rates [2]. Several methods have been proposed in literature such as: bubble agitation [4]; micro-encapsulation [5]; metal-matrix insertion [6]; high-conductivity particle dispersion [7]; nano-particle addition [8]; PCM mixture [9] and metal foam immersion [10]. Among these methods, the application of extended surfaces presents good results for improving the PCM melting rate [1].

Annular arrangements are widely used in thermal systems due to less heat loss than other configurations [11]. Thereby, annular section geometries represent more than 70% of LHTES publications. The ratio between the hull and the tube's diameter is linked to the energy storage capacity and the phase change rate of the material. In this configuration, longitudinal, radial, or pin-shaped fins can be used. Among these, the longitudinal fins are the most widespread, probably due to the ease of design and manufacture while providing high heat exchange efficiency [12].

Several studies have already been conducted on the effect of the geometry of annular section LHTES. Darzi, Farhadi, and Sedighi [13] and Pahamli et al. [14-15], for example, investigated the effect of the eccentricity of tubes in annular sets. Al-Abidi et al. [16], Mat et al. [17], and Rathod and Banerjee [18] found improvement in the efficiency of LHTES with multiple longitudinal fins. New fin geometries have been proposed by Abdulateef et al. [19] and Sciacovelli, Gagliardi, and Verda [20]. Variations in the geometry of the tube itself were tested by Darzi, Jourabian, and Farhadi [21]. Wang et al. [22] and Yuan et al. [23] presented the effect of the fins tilt angle. Mahdi

and Nsofor [24-25] studied the use of fins in a system with nanoparticles. The effect of the length of the fins was addressed by Ji et al. [26]. Optimization studies and innovative longitudinal fin configurations were presented by Deng et al. [27] and Mahdi et al [28-29].

Finned cylindrical cavities filled with PCM have already proven to be effective and meet practical needs. Although there are different proposals for improvement, the fins proportions variation effect, in the PCM melting process, has not yet been explored in other studies. Thus, this work aims to analyze the effect of the fins proportions and arrangements on the lauric acid melting process, inside an annular cavity, using bi-dimensional computational fluid dynamics.

2 Problem Presentation

The studied heat exchanger has an annular section with internal radius (R_{int} = 20 mm) and external radius (R_{ext} = 40 mm). The fins have a length (l_f) and thickness (e_f). The annular cavity is filled with lauric acid, initially in the solid-state. As shown in Figs. 1(a-b), ware studied two fins arrangements: horizontal and vertical, respectively.

Total melting time (t_m) is the usual performance indicator for latent energy systems. As shown in the flowchart of Fig. 2, the dimensional definition of the fins intent to evaluate the design concerning the best efficiency of the system.

The transversal areas of the fins (A_f) and cavity (A_{se}) are obtained by Eq. (1) and (2), respectively, considering the heat exchanger with the annular section shown in Fig. 1. The cavity area is constant in all cases. The area of the fins varies according to the different proportions of occupation (ϕ) obtained by Eq. (3). The degrees of freedom and parameters of the system are defined by the aspect ratio (AR), according to Eq. (4), where $\Delta R = R_{ext} - R_{int}$:

$$A_f = H_f \; e_f \tag{1}$$

$$A_{se} = \pi(R_{ext}^2 - R_{int}^2) \tag{2}$$

$$\phi = \frac{A_f}{A_{se}} \tag{3}$$

$$AR = \frac{l_f}{\Delta R}\,. \tag{4}$$

Initially, 5 different values of ϕ were defined: 0.003, 0.005, 0.01, 0.02 and 0.03. Also, 5 values of *AR* were defined: 1/8, 1/4, 1/2, 3/4, and 7/8. Since A_{se} is constant, 5 different values of A_f were obtained from Eq. (3). For each value of ϕ, 5 vertical fins and 5 horizontal fins were studied, and the values of l_f were obtained from eq. (4). Thus, e_f was obtained as $e_f = A_f / L_f$. All the dimensions analyzed are shown in Tab. 1. However, e_f value for *AR* = 1/8 and ϕ = 0.02 and 0.03 is not physically viable, as it exceeds the value of ΔR.

The lauric acid is a saturated fatty acid used on an industrial scale. It is characterized by biodegradability, chemical stability, non-toxicity, high availability, and low cost. Besides, it presents a small volumetric variation during phase change [30-31]. Table 2 present the thermophysical properties of lauric acid, with the values of specific heat (c_p), latent heat (L), melting temperature (T_m), thermal conductivity (k), thermal expansion coefficient (ζ), density (ρ), and dynamic viscosity (μ).

2.1 Mathematical Model

The mathematical model is composed of the equations of continuity (5), momentum (6), and energy conservation (7) plus the *enthalpy-porosity* phase change model (8-12) of Voller e Prakash [32].

$$\frac{\partial \rho}{\partial t} + \nabla\left(\rho \vec{V}\right) = 0 \tag{5}$$

$$\frac{\partial \rho \vec{V}}{\partial t} + \nabla\left(\rho \vec{V}\vec{V}\right) = -\nabla p + \nabla\left(\mu \nabla \vec{V}\right) + \rho \vec{g} + \vec{S} \tag{6}$$

$$\frac{\partial (\rho \lambda)}{\partial t} + \nabla\left(\rho \vec{V} \lambda\right) = \nabla(k \nabla \mathrm{T}), \tag{7}$$

Where t is the time, p is the pressure, $\vec{g}$ is the acceleration of gravity, λ is the total enthalpy, $\vec{V}$ is the velocity vector, ρ is the density, and $\vec{S}$ is the source term given by Eq. (8)

$$\vec{S} = \frac{(1-\gamma)^2}{(\gamma^3+\varepsilon)} C\vec{V}. \quad (8)$$

In Eq. (8), $\varepsilon = 0.001$ is a constant, to avoid division by zero, C is the constant of the porous zone, related to its morphology [32], γ is the volume fraction of solid and liquid, obtained through Eq. (9),

$$\gamma = \begin{cases} 0 & se \quad T < T_s \\ 1 & se \quad T > T_l \\ \frac{T-T_s}{T_l-T_s} & se \quad T_s < T < T_l \end{cases} \quad (9)$$

where T_s is the temperature of the solid and T_l the temperature of the liquid.

The total enthalpy (λ) is obtained by adding the sensitive enthalpy (λ_{sen}) and the variation of the enthalpy in the phase change (λ_L). The sensitive enthalpy (λ_{sen}) is given by Eq. (10):

$$\lambda_{sen} = \lambda_{ref} + \int_{T_{ref}}^{T} C_p dT \quad (10)$$

Where c_p is the specific heat at constant pressure, and λ_{ref} is the enthalpy at the reference temperature (T_{ref} = 293.15 K). The variation in enthalpy in the phase change (λ_L) is a function of temperature, obtained by Eq. (11) or by Eq. (12)

$$\lambda_L = \gamma L \quad (11)$$

$$\lambda_L = \begin{cases} 0 & if \quad T < T_s \\ L & if \quad T > T_l \\ \gamma L & if \quad T_s < T < T_l \end{cases} \quad (12)$$

2.2 Initial and Boundary Conditions

The initial conditions consisted of $V\,(x,y,0) = 0\;and\;\;T(x,y,0) = 20°C$. The boundary conditions used were:

$$T\,|_{\frac{r}{\theta}=R_{in}} = T_w \qquad V\,|_{\frac{r}{\theta}=R_{in}} = 0 \tag{13}$$

$$q''\,|_{\frac{r}{\theta}=R_{ex}} = 0 \qquad V\,|_{\frac{r}{\theta}=R_{ex}} = 0 \tag{14}$$

where T_w = 80 ºC and q''_w are the temperature and the heat flow in the wall, respectively. The following boundary conditions were considered in the fin walls:

$$T = T_w = 80°C \text{ and } V = 0 \tag{15}$$

2.3 Numerical Method and Validation

The simulations were performed in ANSYS Fluent software 18.2. The pressure was defined as *PRESTO,* the *SIMPLE* method was used for the pressure-velocity coupling and the gradient of spatial discretization as *Least Squares Cell-Based.* The relaxation factors used for pressure, density, field forces, momentum, liquid fraction, and energy were, respectively: 0.3; 1.0; 0.5; 0.5; 0.6 and 1.0. The energy and momentum were established as *Second-Order Upwind*. With a limit of 1000 interactions per time step, the time step was 0.01 s. The absolute convergence criterion established was 10^{-6} for mass and velocity and 10^{-8} for the energy equation.

The continuous growth of publications related to CFD and the significant advances in computational techniques and technologies have also improved methods for validating results, ensuring the credibility of works involving computational fluid dynamics. Among the mesh validation methods, GCI (Grid Convergence Index) is credible and recommended, having been proven through hundreds of cases [33]. Three computational meshes were created (*M1, M2, M3*), with 28457, 14520, and 10118 volumes respectively, applying this methodology. GCI was calculated for each mesh and evaluated. For *M1*, GCI had an average value of 0.003%, affirming the

quality of this mesh. Mesh *M1* is composed of quadrilateral elements and is shown in Fig. 3. Also seen in Fig. 3 is the great mesh refinement in active surfaces: Detail (A) shows the refining gradient on the fin walls while Detail (B) shows the refinement of the elements close to the inner cylinder wall. All meshes used in the study of fin aspect ratio followed the same criteria of distribution and refinement of the elements.

For numerical validation, experimental data of Al-Abidi et al. [34] and Yuan et al. [23] were used. Both cases are for an annular heat exchanger with internal fins, filled with PCM. Quantitative analysis of the Al-Abidi et al. [34] data was performed using the values of local temperature (*T*) as a time (*t*) function. Fig. 4 shows an approximate temperature behavior between the present work and the experimental data. The average percentage difference between both is 4.9%. This is a relatively small difference because it is a local temperature value. Quantitative analysis of the Yuan et al. [23] data was performed using the values of the liquid fraction (β) as a function of the Fourier number ($Fo = \alpha\, t/L_c^2$), where α = 7.53.10^{-8} m^2/s is the thermal diffusivity, and *Lc* = 0.04 m is the characteristic length established by the author. A comparison of the results obtained by this work and those presented by the reference are shown in Fig. 5. It presents an average percentage difference of approximately 1.5%, which proves a good agreement between results.

Qualitative analysis comparing the results from this work and Yuan et al. [23] is shown in Figs. 6(a-b), respectively. The figures present the β fields at different melting stages, where the blue and red represent the solid and the liquid phase of the PCM, respectively. Regardless of running time, the similarity between results was significant, showing the satisfactory agreement of the numerical model.

As previously presented, the mesh analysis revealed a very low GCI, giving credibility to the results. A triple validation with experimental data from two different authors was presented. In view of the great results obtained, the model was considered validated and adequate for the case study.

3 Results and Discussions

In the initial moments of the melting process, heat transfer is predominantly through conduction due to the solid layer's direct contact with the heated wall. As the liquid layer forms between the heated wall and the solid, the participation of natural convection in the heat transfer process increases. This process is shown in Figs. 7(a-

b) for AR = 7/8 and ϕ = 0.003 in systems with vertical and horizontal fins, respectively. The right side of the section shows streamlines, and the left side shows temperature fields. The streamlines are superimposed on the liquid fraction plane, where the black color indicates the solid phase and white the liquid phase. The Details shown in Figs. 7(c-h) present the velocity vectors.

The left side of Figs. 7(a-b) shows contours of the temperature of the phase-change process. In the vertical fin geometry of Fig. 7(a), a temperature gradient can be seen in the solid phase (blue to yellow/green). This gradient occurs because the PCM is sub-cooled at the initial condition. In the liquid region (red), horizontal thermal stratification is observed. Temperature gradients are also seen close to the solid-liquid interface and the internal wall of the exchanger, depicting a tendency of upward drag along the internal and descending walls and near the solid-liquid interface. This behavior is confirmed in the vectors shown in Figs. 7(c-d), where ascending and descending convective currents can be observed. Upward convective currents are a direct result of the buoyancy from the reduction of the PCM density as the internal surface of the exchanger is heated concerning the PCM. Note that a downward convective current must also be present to preserve the conservation of the mass, as verified.

In this work, the number of Rayleigh was defined as $Ra = \left[g\ \zeta\ {L_c}^3\ (T_w - T_m)\right] / (\upsilon\ \alpha)$, where υ is the kinematic viscosity. Since the temperature and the characteristic length ($Lc = R_{ext}$) are the same for all cases studied, Ra = 34364. This value is greater than the critical Rayleigh (Ra_{cr} = 12250) presented by Yigit et al. [35], to an equivalent annular geometry, which justifies the appearance of Rayleigh-Bénard cells. In the horizontal fin geometry of Fig. 7(b) temperature contours also show a thermal gradient in the solid phase as per the initial sub-cooled state. However, the liquid phase has a diffuse temperature gradient. Such behavior is following the expected Rayleigh-Bénard convective behavior of a heated surface. This fact becomes evident from characteristic recirculations of the Rayleigh-Bénard behavior shown by the streamlines over the horizontal heated surfaces, as well as vectors of Figs. 7(e, g). In this convective process, the heated liquid rises in multiple regions perpendicular to the heat source, coming into contact and fusing the solid interface as it exchanges heat and cools. Due to the conservation of mass, cooled liquid moves downwards towards the heated plane, establishing a recirculation zone and an efficient thermal exchange cycle. Fig. 7(f) shows an upward flow near the heated surface of the tube and

consequently, downward flow due to the presence of Rayleigh-Bénard cells at the top of the cavity. The shear region between ascending and descending flows can also be seen in Fig. 7(h). This resulting intense thermal exchange system persists if there is a solid material in the region above the heated surfaces.

The evolution of the melting process for a sample of the studied cases is shown in Figs. 8(a-e), where the liquid-solid interfaces can be observed at 1 min, 10 min, 20 min, 30 min, 40 min, and 60 min. It is possible to observe the progress of cases with *AR* = 1/4, 1/2 and 7/8 for all ϕ, both in terms of melting and the geometric aspect evolution with the variation of *AR* and ϕ. The first three columns cover cases with vertical fins, while the last three refer to cases with horizontal fins. Observing the lines for horizontal fins at *t* = 1 min, 10 min, and 20 min, the liquid region advances significantly in comparison to the respective cases with vertical fins. This trend is in line with the natural convection process shown in Fig. 7.

The liquid fraction lines of Figs. 8(a-e) at *t* = 30 min, 40 min, and 60 min show a deceleration in the melting speed of the cases with horizontal fins compared to vertical fins as the solid phase moves away from heated surfaces. It is noted that the total melting process concluded before 40 min for the vertical fin, while for the horizontal fin, the melting process extends beyond the 60 min when analyzing specifically the cases with AR = 7/8 of Fig. 8(e).

Figures 9(a-e) shows the variation of β vs. Fourier number ($Fo = \alpha\, t/L_c^2$), for horizontal and vertical fins with *AR* = 7/8, 3/4, 1/2, 1/4, and 1/8 for ϕ = 0.003, 0.005, 0.01, 0.02, and 0.03. In this work, the characteristic length was defined as $L_c = R_{ext}$. Figures 9(a-e) shows that for all cases up to approximately *Fo* = 0.006, the values of β are practically superimposed before drifting apart as *Fo* increases. Between *Fo* = 0.006 and *Fo* = 0.05, melting is favored by horizontal fins, with the faster melting process occurring in the fin with *AR* = 7/8 for all the values of ϕ. From *Fo* = 0.05 and higher, there is a transition in the slope of the horizontal fins, with the reduction of the melting rate in these configurations. Afterward, vertical fins complete the melting process ahead of horizontal fins starting from the highest *AR* = 7/8 and proceeding in an orderly way to the lowest *AR* = 1/8. Only after the total melting of all cases with vertically oriented fins, the cases with horizontally oriented fins begin to reach β = 1, also in an orderly manner, from the cases with the highest *AR*, down to the lowest. This behavior of β is similar for all ϕ values, with only a subtle increase in the melting rate as ϕ increases.

Figures 10(a-c) present the liquid fraction fields (right side) and temperature fields (left side) at t = 600 s and 2270 s, for ϕ = 0.03 and AR = 7/8, 1/2 and 1/4, respectively. The initial instant (600 s) enables us to view the heat exchange mechanisms present at the beginning of the melting process, while the final instant (2270 s) refers to the total melting time of the fastest case (vertical fins with AR = 7/8). This observation allows a comparison of the other cases melting state at the same instant as when the fastest case had already concluded. The β value is displayed at the center of each geometry. Observing the temperature fields at t = 600 s, it is visible the greater dynamism of the cases with horizontal fins as the weaving outlines are consistent with recirculations of the Rayleigh-Bénard convective behavior. In contrast, in the cases with vertically oriented fins, it is possible to observe relatively stratified temperature fields and upward flow behavior only in the region close to the fins and the heated wall. Consequently, the β value is higher for cases with horizontal fins.

Still, concerning Figs. 10(a-c) at t = 2270 s, it can be seen in all cases that the temperature fields show a well-defined thermal step between solid and liquid phase despite presenting a small thermal stratification close to the solid-liquid interface. However, when comparing the β values between vertical and horizontal fins, it is observed that the vertical fins have a higher melting rate than the horizontal fins because the vertical fins are closer to the solid mass, compared to the horizontal fins.

Figures 11(a-e) shows the behavior of the Nusselt number $\left(\overline{Nu} = \bar{h}\,.\,\mathrm{Lc}/k_l\right)$ as a function of *Fo,* for horizontal and vertical fins with AR = 7/8, 3/4, 1/2, 1/4, and 1/8 for ϕ = 0.003, 0.005, 0.01, 0.02, and 0.03. The average heat transfer coefficient $\left[\bar{h} = q"/\,(T_w - T_m)\,\right]$ is calculated from is the total heat flow (q") while the temperatures are taken as T_w = 80°C at the active wall and T_m = 44.2°C as the melting temperature of the PCM. Figures 11(a-e) can be divided into three behavior patterns indicated by I, II, and III. As observed by Ji et al. [26], these patterns are related to the heat exchange mechanisms during the phase change of the PCM. In addition to the analysis of *Nu* values, Figs. 12(a-c) shows the fields of temperature, liquid fraction, and streamlines of an example case. The joint analysis of Figs. 11(a-e) with Figs. 12(a-c) allows better compression of the three-behavior described below. Region I start with $\overline{Nu}$ higher than 12 for all cases. This fact is due to the process beginning when there is direct contact between the solid PCM and the heat source. As the PCM melts, the liquid interface is formed between the solid and the heat source. The increasing size of the liquid layer

increases the thermal resistance by conduction between the heated wall and the melting material with a gradual decrease to *Fo* = 0.003, as can be observed in the Fig. 12(a). Region II is characterized by the beginning of fluctuations in the behavior of $\overline{Nu}$. These fluctuations are due to a further increase in the liquid layer's size and the beginning of an intense convective process, which can be observed in the streamlines of the Fig. 12(b). The greater dynamism of the convective process on the horizontally oriented fins, its due the Rayleigh-Bénard convective pattern. In line with this phenomenon, the highest values of $\overline{Nu}$ that occur in this region are relative to the horizontal fins (dashed lines). In region III, from *Fo* = 0.05, $\overline{Nu}$ decreases rapidly for cases with a horizontal fin. As shown in Fig. 12(c), this behavior makes the heat transfer process restricted to a practically conductive in the molten and stationary liquid. As the melting process approaches the end, cases with vertically oriented fins presents a gradual drop in the value of $\overline{Nu}$, until zero. This behavior of Nu is similar for all ϕ values, with only a subtle increase in region II, according to the increase in ϕ.

One way to qualify the different systems analyzed is by their effectiveness (η_f) in relation to the system without fins. In this work, this effectiveness is defined as: $\eta_f = (\beta/\beta_0) - 1$, where β_0 is the liquid fraction of a case without fins at the same instant in time. Figures 13(a-e) shows the variation of η_f as a function of *Fo* for vertical and horizontal fins with *AR* = 1/8, 1/4, 1/2, 3/4, and 7/8 for ϕ = 0.003, 0.005, 0.01, 0.02, and 0.03. It is initially observed that all cases present their highest η_f at the beginning of the melting process. Ideally, η_f would remain high throughout the melting process. However, the cases show two patterns of decrease, first more accentuated and then gradually. The effectiveness of horizontal and vertical fins, represented by dotted and continuous lines, respectively, is quantitatively similar for each value of *AR*. The value of η_f is initially higher for horizontal fins, but for *Fo* > 0.06, vertical fins become more efficient. This inversion occurs for all AR presented. Horizontal fins have η_f tending to 0 with increasing *Fo*. This tendency indicates the fins' inefficiency in the melting process since the null value of η_f is equivalent to a system without fins. However, vertical fins keep the η_f value practically stable between *Fo* = 0.06 and the ending of the melting process. For these geometries, higher *AR* values reveal greater effectiveness and lower *Fo* value after the melting process. The η_f behavior is equivalent to all ϕ values, with a directly proportional increase between the η_f and ϕ values.

Figures 14(a-b) show the time to reach complete melting (t_m) as a function of *AR*, for horizontal and vertical fins, respectively, with ϕ = 0.003, 0.005, 0.01, 0.02 and 0.03. For better visualization of the results, the t_m range is different between the cases. Figures 14(a-b) shows that for both horizontal and vertical fins, the decrease in t_m is practically linear with *AR*.

For cases with horizontal fins, Fig. 14(a) shows a decrease in t_m with an increase in *AR* below 1000 s for all values of ϕ. This small period indicates the low representativeness of the aspect ratio in the total melting time when the fins are arranged horizontally. This fact is related to what is observed in Figs. 13(a-e), where it can be observed that η_f is practically null, for all *AR* values at the end of the melting process of the cases with horizontal fins. Even if cases with horizontal fins promote a higher melting rate at the beginning of the process, the conclusion of the melting process stretches further due to the gap between the solid PCM and the heat source. Increases in *AR* in horizontal fins do not reduce this gap.

The total melting time of cases with vertical fins of Fig. 14(b) varies between 2000 s and 8000 s. The higher amplitude in this ordinate axis is due to the more significant influence of the *AR* variation on the total melting time. As seen in Figs. 13(a-e), the increase in *AR* results in greater effectiveness at the end of the melting process for vertical fins. Since vertical fins maintain proximity between the heat source and the solid PCM until the end of the melting process, increases in *AR* also increase the proximity of the heated wall to the solid PCM.

As seen in Figs. 14(a-b), the shortest total melting time ($t_{m,min}$) occurs for *AR* = 0.88 (7/8). In these figures, although the tendency of $t_{m,min}$ to decrease with increasing ϕ can be observed, a more accurate assessment is shown in Figs. 15(a-b), which show the variation of $t_{m,\min}$ as a function of ϕ, for horizontal and vertical fins, respectively, at the shortest melting time of *AR* = 0.88. Figures 15(a-b) demonstrate that $t_{m,min}$ is inversely proportional to ϕ regardless of the fin layout. This can be due to the volume reduction of PCM in the cavity since the increase in ϕ implies an increase in the volume occupied by the fin. It is also observed that the range of variation of $t_{m,min}$ is higher for vertical fins (Fig.15(b)) than for horizontal fins (Fig. 15(a)). The difference between the time ranges is the result of prolonged load cycles in systems with horizontal fins and shorter cycles in systems with vertical fins, as seen in Figs. 14(a-b).

5 Conclusions

This work sought to analyze the behavior of the melting process of lauric acid PCM in a cylindrical cavity concerning the dimensional variation fins. The numerical model was validated with numerical and experimental results provided by literature. The computational mesh analysis was performed using the GCI method, which resulted in an average value of 0.003%. Under these conditions, the main results were:

- Horizontal fins had a melting rate up to 15% higher than vertical fins if there was solid PCM in the region above the layer of PCM already fused next to the horizontal fin. This occurred for all values of ϕ and was due to localized Rayleigh-Bénard convective effect;
- For all values of ϕ, the total time for complete melting was, on average, 44% lower for vertical fins than for horizontal fins. In a vertical fin configuration, buoyancy effects were less pronounced in the active wall (circular internal) and the vertical fin. Consequently, this region was the last to be melted, and higher temperature differences develop between PCM and active walls, promoting higher rates of heat transfer throughout the melting process;
- Increases of the aspect ratio, or thinness, of the fin, reduced the time of the total melting process by the maximum values of 11.3% for vertical fins and 1.2% for horizontal fins, with ϕ = 0.003;
- Increases in ϕ resulted in an approximately linear decrease in the total melting time of the PCM in the heat exchanger. This was due to the larger area of the fin's occupancy in the cavity.

Acknowledgments

We thank FAPERGS (Research Support Foundation of the State of Rio Grande do Sul – Process: 2270-25.51/14-8), The National Council of Scientific and Technological Development (CNPq – Process: 307791/2019-0), and the Italian Ministry for Education, University and Research, for their support in carrying out this research.

REFERENCES

[1] L. Kalapala, J.K. Devanuri, Influence of operational and design parameters on

443 the performance of a PCM based heat exchanger for thermal energy storage –
444 A review, J. Energy Storage. 20 (2018) 497–519.
445 [2] G. Alva, Y. Lin, G. Fang, An overview of thermal energy storage systems,
446 Energy. 144 (2018) 341–378. https://doi.org/10.1016/j.energy.2017.12.037.
447 [3] J. Jaguemont, N. Omar, P. Van den Bossche, J. Mierlo, Phase-change materials
448 (PCM) for automotive applications: A review, Appl. Therm. Eng. 132 (2018) 308–
449 320. https://doi.org/10.1016/j.applthermaleng.2017.12.097.
450 [4] R. VELRAJ, R. V. SEENIRAJ, B. HAFNER, C. FABER, K. SCHWARZER,
451 Experimental analysis and numerical modelling of inward solidification on a
452 finned vertical tube for a latent heat storage unit, Sol. Energy. 60 (1997) 281–
453 290.
454 [5] M.N.A. Hawlader, M.S. Uddin, M. Mya, Microencapsulated PCM thermal-energy
455 storage system, Appl. Energy. 74 (2003) 195–202.
456 [6] J.P. Trelles, J.J. Dufly, Numerical simulation of porous latent heat thermal energy
457 storage for thermoelectric cooling, Appl. Therm. Eng. 23 (2003) 1647–1664.
458 https://doi.org/10.1016/S1359-4311(03)00108-X.
459 [7] E.S. Mettawee, G.M.R. Assassa, Thermal conductivity enhancement in a latent
460 heat storage system, Sol. Energy. 81 (2007) 839–845.
461 https://doi.org/10.1016/j.solener.2006.11.009.
462 [8] S.F. Hosseinizadeh, A.A.R. Darzi, F.L. Tan, Numerical investigations of
463 unconstrained melting of nano-enhanced phase change material (NEPCM)
464 inside a spherical container, Int. J. Therm. Sci. 51 (2012) 77–83.
465 https://doi.org/10.1016/j.ijthermalsci.2011.08.006.
466 [9] A. Sari, K. Kaygusuz, Thermal performance of a eutectic mixture of lauric and
467 stearic acids as PCM encapsulated in the annulus of two concentric pipes, Sol.
468 Energy. 72 (2002) 493–504.
469 [10] A. Atal, Y. Wang, M. Harsha, S. Sengupta, Effect of porosity of conducting matrix
470 on a phase change energy storage device, Int. J. Heat Mass Transf. 93 (2016)
471 9–16. https://doi.org/10.1016/j.ijheatmasstransfer.2015.09.033.
472 [11] F. Agyenim, P. Eames, M. Smyth, Heat transfer enhancement in medium
473 temperature thermal energy storage system using a multitube heat transfer
474 array, Renew. Energy. 35 (2010) 198–207.
475 https://doi.org/10.1016/j.renene.2009.03.010.
476 [12] A.M. Abdulateef, S. Mat, J. Abdulateef, K. Sopian, A.A. Al-Abidi, Geometric and

477 design parameters of fins employed for enhancing thermal energy storage
478 systems: a review, Renew. Sustain. Energy Rev. 82 (2018) 1620–1635.
479 https://doi.org/10.1016/j.rser.2017.07.009.
480 [13] A.R. Darzi, M. Farhadi, K. Sedighi, Numerical study of melting inside concentric
481 and eccentric horizontal annulus, Appl. Math. Model. 36 (2012) 4080–4086.
482 https://doi.org/10.1016/j.apm.2011.11.033.
483 [14] Y. Pahamli, M.J. Hosseini, A.A. Ranjbar, R. Bahrampoury, Inner pipe downward
484 movement effect on melting of PCM in a double pipe heat exchanger, Appl. Math.
485 Comput. 316 (2018) 30–42. https://doi.org/10.1016/j.amc.2017.07.066.
486 [15] Y. Pahamli, M.J. Hosseini, A.A. Ranjbar, R. Bahrampoury, Analysis of the effect
487 of eccentricity and operational parameters in PCM-filled single-pass shell and
488 tube heat exchangers, Renew. Energy. 97 (2016) 344–357.
489 https://doi.org/10.1016/j.renene.2016.05.090.
490 [16] A. a. Al-Abidi, S. Mat, K. Sopian, M.Y. Sulaiman, A.T. Mohammad, Numerical
491 study of PCM solidification in a triplex tube heat exchanger with internal and
492 external fins, Int. J. Heat Mass Transf. 61 (2013) 684–695.
493 https://doi.org/10.1016/j.ijheatmasstransfer.2013.02.030.
494 [17] S. Mat, A.A. Al-abidi, K. Sopian, M.Y. Sulaiman, A. Th, Enhance heat transfer
495 for PCM melting in triplex tube with internal – external fins, Energy Convers.
496 Manag. 74 (2013) 223–236.
497 [18] M.K. Rathod, J. Banerjee, Thermal performance enhancement of shell and tube
498 Latent Heat Storage Unit using longitudinal fins, Appl. Therm. Eng. 75 (2015)
499 1084–1092. https://doi.org/10.1016/j.applthermaleng.2014.10.074.
500 [19] A.M. Abdulateef, S. Mat, K. Sopian, J. Abdulateef, A.A. Gitan, Experimental and
501 computational study of melting phase-change material in a triplex tube heat
502 exchanger with longitudinal/triangular fins, Sol. Energy. 155 (2017) 142–153.
503 https://doi.org/10.1016/j.solener.2017.06.024.
504 [20] A. Sciacovelli, F. Gagliardi, V. Verda, Maximization of performance of a PCM
505 latent heat storage system with innovative fins, Appl. Energy. 137 (2015) 707–
506 715. https://doi.org/10.1016/j.apenergy.2014.07.015.
507 [21] A.A. Rabienataj Darzi, M. Jourabian, M. Farhadi, Melting and solidification of
508 PCM enhanced by radial conductive fins and nanoparticles in cylindrical annulus,
509 Energy Convers. Manag. 118 (2016) 253–263.
510 https://doi.org/10.1016/j.enconman.2016.04.016.

511 [22] P. Wang, H. Yao, Z. Lan, Z. Peng, Y. Huang, Y. Ding, Numerical investigation of
512 PCM melting process in sleeve tube with internal fins, Energy Convers. Manag.
513 110 (2016) 428–435. https://doi.org/10.1016/j.enconman.2015.12.042.
514 [23] Y. Yuan, X. Cao, B. Xiang, Y. Du, Effect of installation angle of fins on melting
515 characteristics of annular unit for latent heat thermal energy storage, Sol.
516 Energy. 136 (2016) 365–378. https://doi.org/10.1016/j.solener.2016.07.014.
517 [24] J.M. Mahdi, E.C. Nsofor, Melting enhancement in triplex-tube latent thermal
518 energy storage system using nanoparticles-fins combination, Int. J. Heat Mass
519 Transf. 109. 109 (2017) 417–427.
520 https://doi.org/10.1615/TFEC2017.est.018280.
521 [25] J.M. Mahdi, E.C. Nsofor, Solidification enhancement of PCM in a triplex-tube
522 thermal energy storage system with nanoparticles and fi ns, Appl. Energy. 211
523 (2018) 975–986.
524 [26] C. Ji, Z. Qin, S. Dubey, F.H. Choo, F. Duan, Simulation on PCM melting
525 enhancement with double-fin length arrangements in a rectangular enclosure
526 induced by natural convection, Int. J. Heat Mass Transf. 127 (2018) 255–265.
527 https://doi.org/10.1016/j.ijheatmasstransfer.2018.07.118.
528 [27] S. Deng, C. Nie, G. Wei, W.B. Ye, Improving the melting performance of a
529 horizontal shell-tube latent-heat thermal energy storage unit using local
530 enhanced finned tube, Energy Build. 183 (2019) 161–173.
531 https://doi.org/10.1016/j.enbuild.2018.11.018.
532 [28] Jasim M. Mahdi, Sina Lohrasbi, Davood D. Ganji, Emmanuel C. Nsofor,
533 Accelerated melting of PCM in energy storage systems via novel configuration
534 of fins in the triplex-tube heat exchanger, Int. J. Heat Mass Transf. 124 (2018)
535 663–676. https://doi.org/10.1016/j.ijheatmasstransfer.2018.03.095.
536 [29] J.M. Mahdi, S. Lohrasbi, D.D. Ganji, E.C. Nsofor, Simultaneous energy storage
537 and recovery in the triplex-tube heat exchanger with PCM , copper fi ns and Al 2
538 O 3 nanoparticles, Energy Convers. Manag. 180 (2019) 949–961.
539 [30] S. POLAT, P. SAYAN, Kinetic analysis and polymorphic phase transformation of
540 glycine in the presence of lauric acid, J. Cryst. Growth. 481 (2018) 71–79.
541 https://doi.org/10.1016/j.jcrysgro.2017.10.037.
542 [31] A. Sarı, K. Kaygusuz, Thermal and heat transfer characteristics in a latent heat
543 storage system using lauric acid Sar, A. and Kaygusuz, K. Energy Conversion
544 and Management, 2002, 43, (18), 2493–2507, Fuel Energy Abstr. 44 (2003)

189–190. https://doi.org/10.1016/S0140-6701(03)82063-5.

[32] V.R. Voller, C. Prakash, A fixed grid numerical modelling methodology for convection-diffusion mushy region phase-change problems, Int. J. Heat Mass Transf. 30 (1987) 1709–1719. https://doi.org/10.1016/0017-9310(87)90317-6.

[33] I.B. Celik, U. Ghia, P.J. Roache, C.J. Freitas, H. Coleman, P.E. Raad, Procedure for Estimation and Reporting of Uncertainty Due to Discretization in CFD Applications, J. Fluids Eng. 130 (2008) 078001. https://doi.org/10.1115/1.2960953.

[34] A.A. Al-Abidi, S. Mat, K. Sopian, M.Y. Sulaiman, A.T. Mohammad, Internal and external fin heat transfer enhancement technique for latent heat thermal energy storage in triplex tube heat exchangers, Appl. Therm. Eng. 53 (2013) 147–156. https://doi.org/10.1016/j.applthermaleng.2013.01.011.

[35] S. Yigit, N. Chakraborty, Numerical investigation of aspect ratio influences on Rayleigh-Bénard convection of power-law fluids in vertical cylindrical annuli, Therm. Sci. Eng. Prog. 9 (2019) 185–199. https://doi.org/10.1016/j.tsep.2018.10.007.

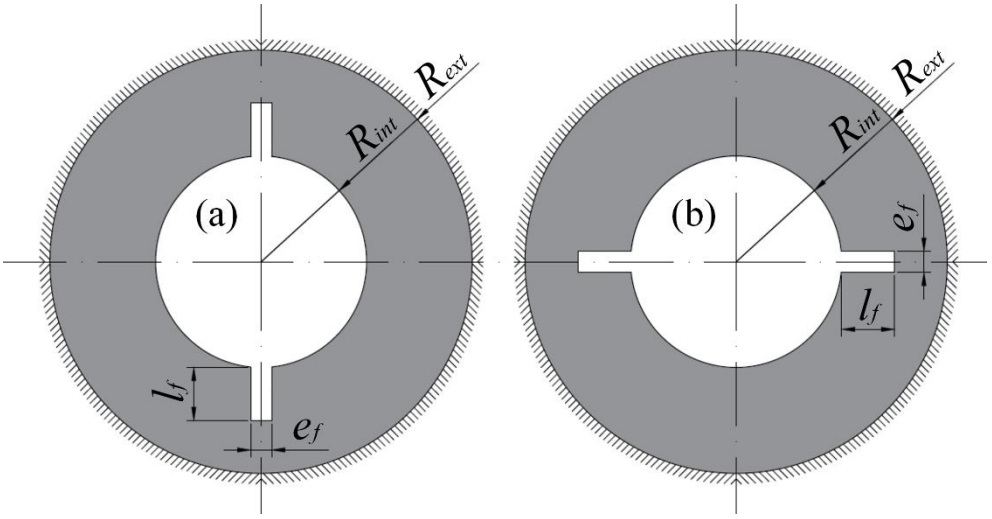

562 Figure 1 - Annular tube with: (a) vertical and (b) horizontal fins.

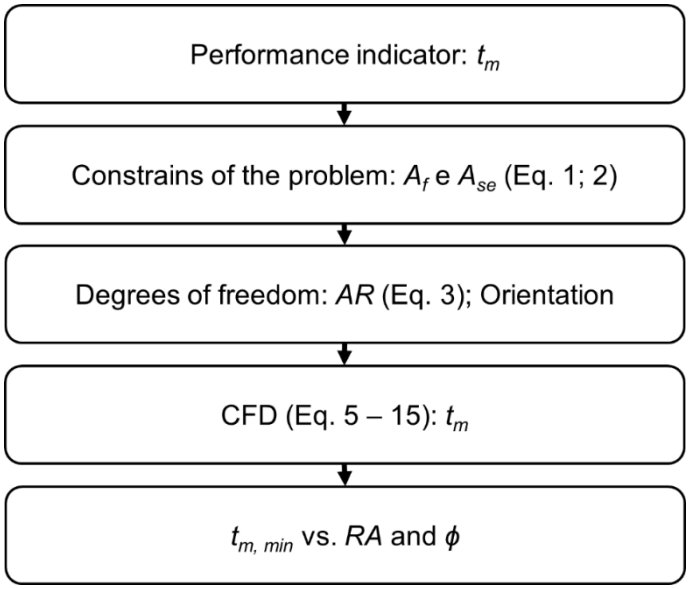

563 Figure 2 – Flowchart of fin studies conducted.

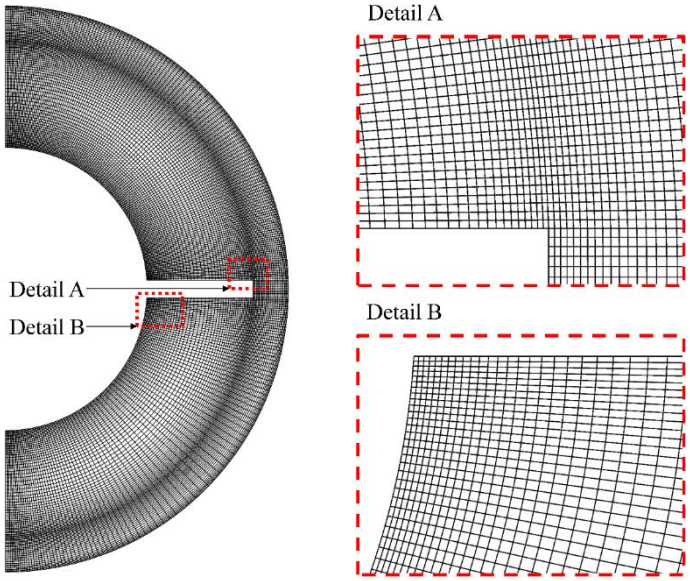

564 Figure 3 – Computational mesh with details at the fin end (A) and the fin base and
565 inner cylinder wall (B).

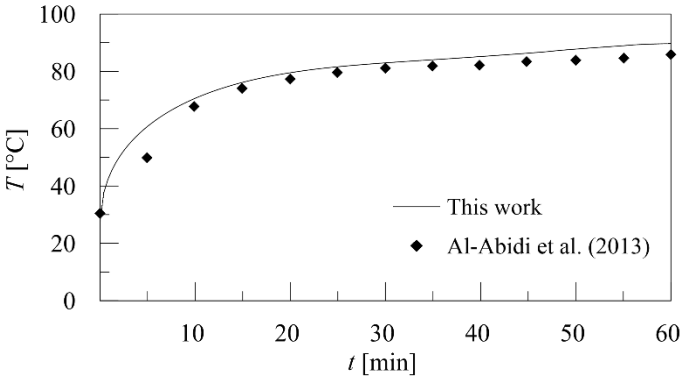

566

Figure 4 – Temperature (*T*) vs. (*t*): current numerical simulation and experimental data from Al-Abidi et al. [23].

567

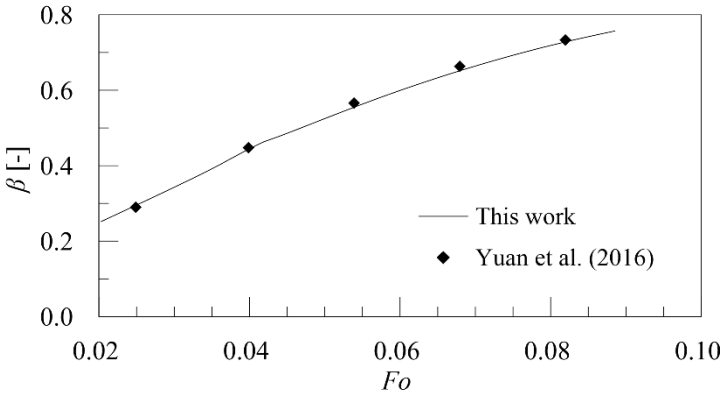

568 Figure 5 – Liquid fraction (*β*) vs. *Fo*: current numerical simulation and experimental
569 data from Yuan et al. [23].

570

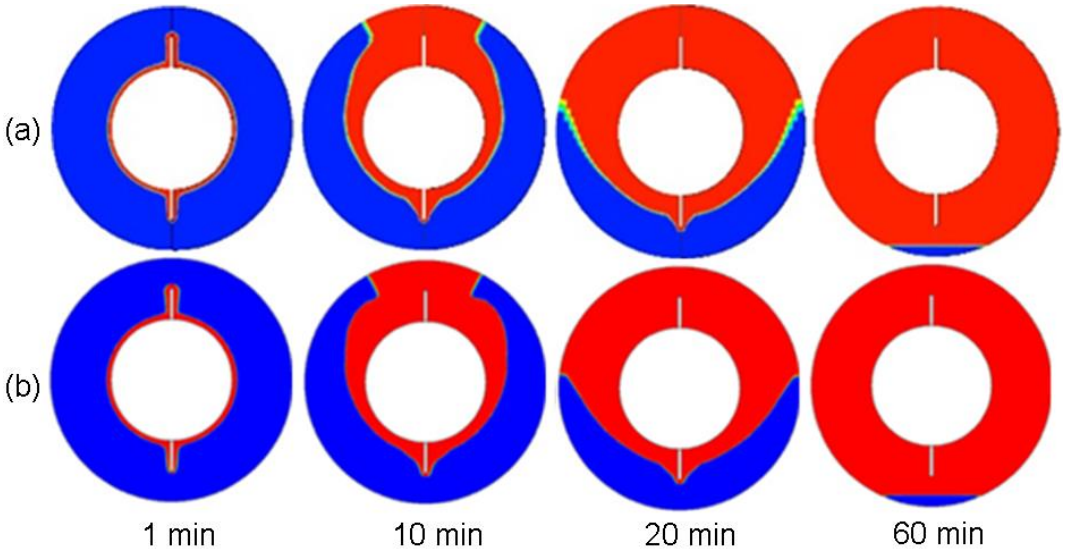

571

572 Figure 6 –β fields at t = 1;10; 20 and 60 min: (a) current numerical simulation and (b)
573 experimental data from Yuan et al. [23].

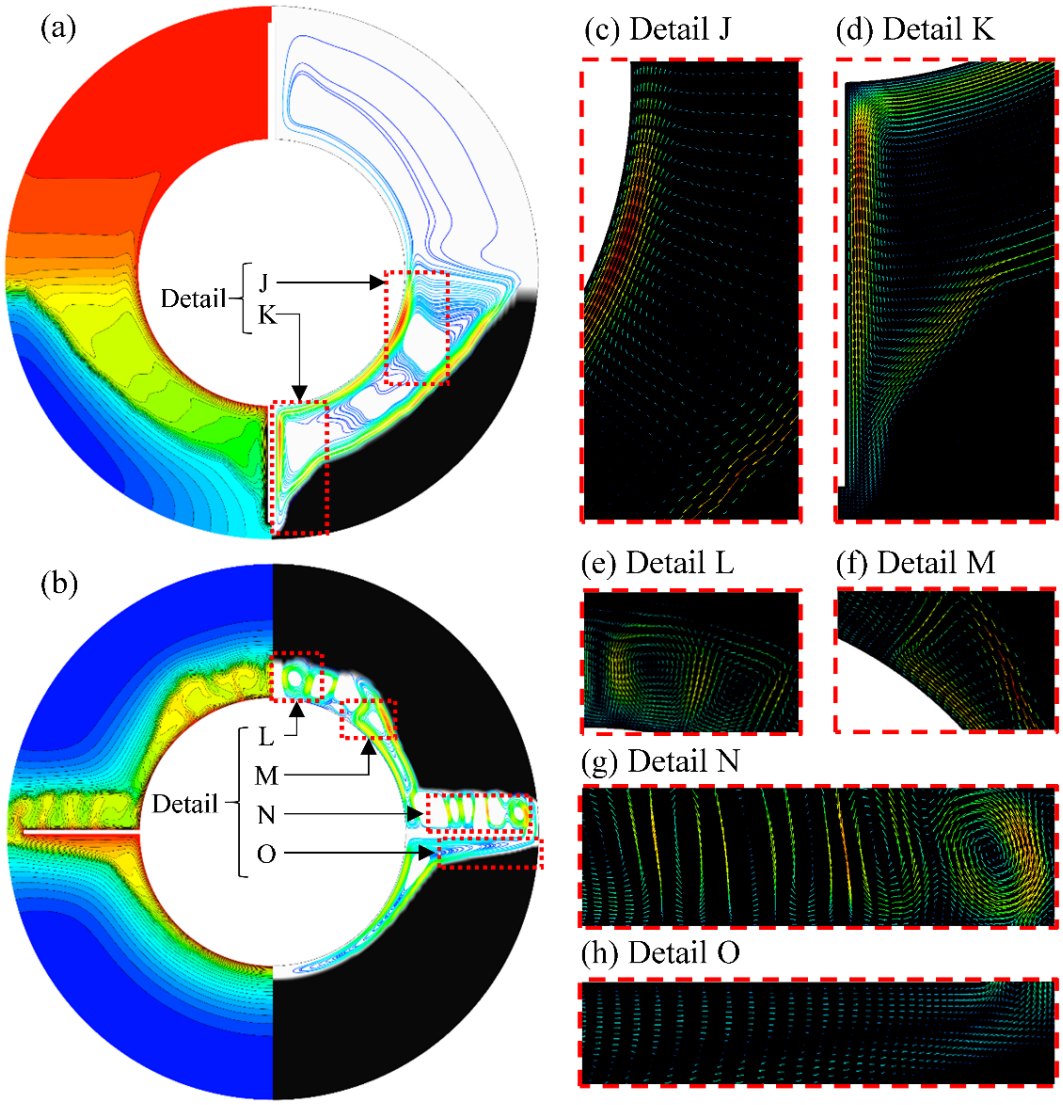

574

575 Figure 7 – T fields and streamlines, with details of the velocity vectors for *AR* = 7/8
576 and ϕ = 0.003: (a) vertical fins, (b) horizontal fins and (c, d, e, f, g, h) related to
577 Details J, K, L, M, N and O respectively.

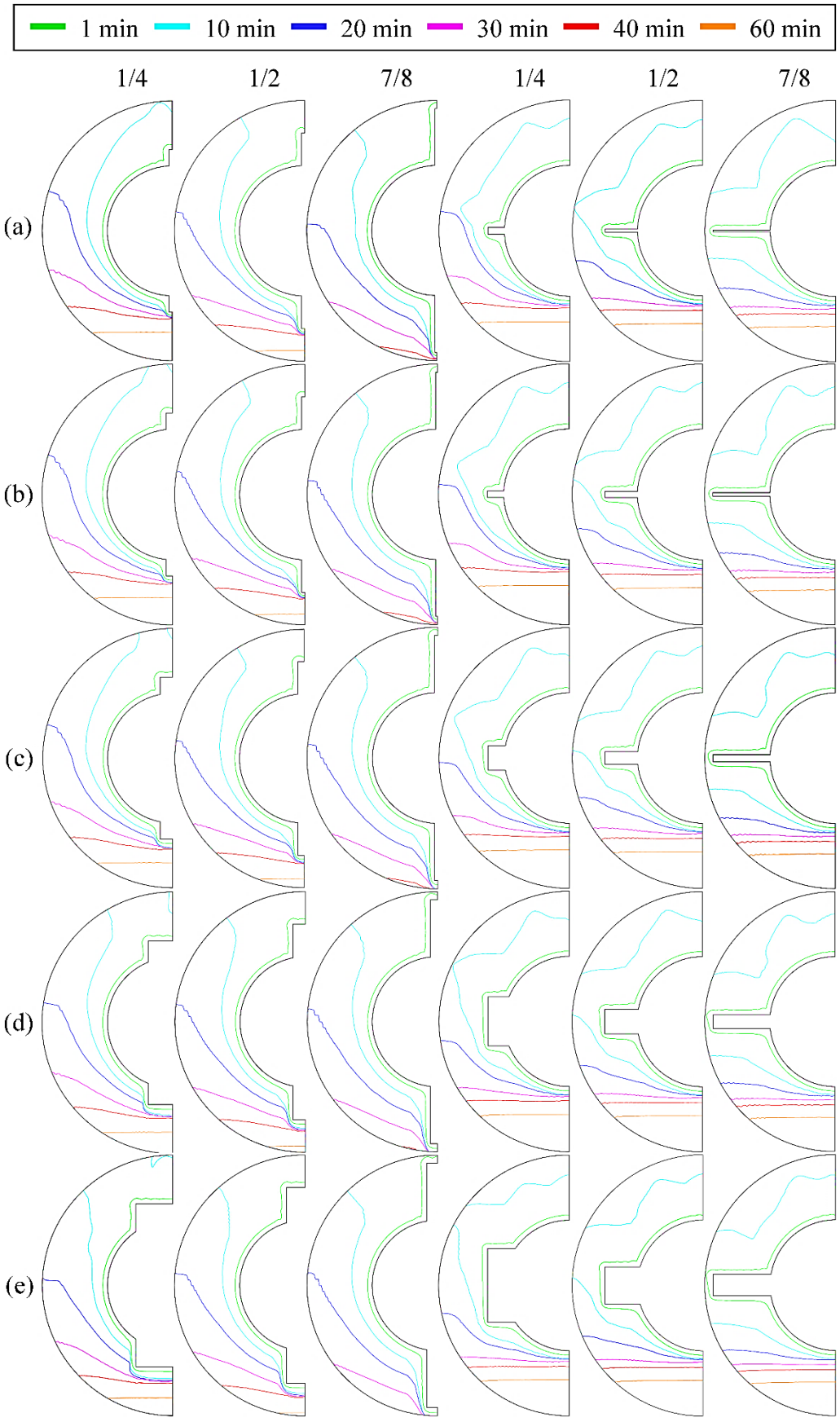

Figure 8 – Solid-liquid interface for different moments of the melting process for *AR* = 1/4, 1/2 and 7/8 and ϕ = (a) 0.003, (b) 0.005, (c) 0.01, (d) 0.02 and (e) 0.03.

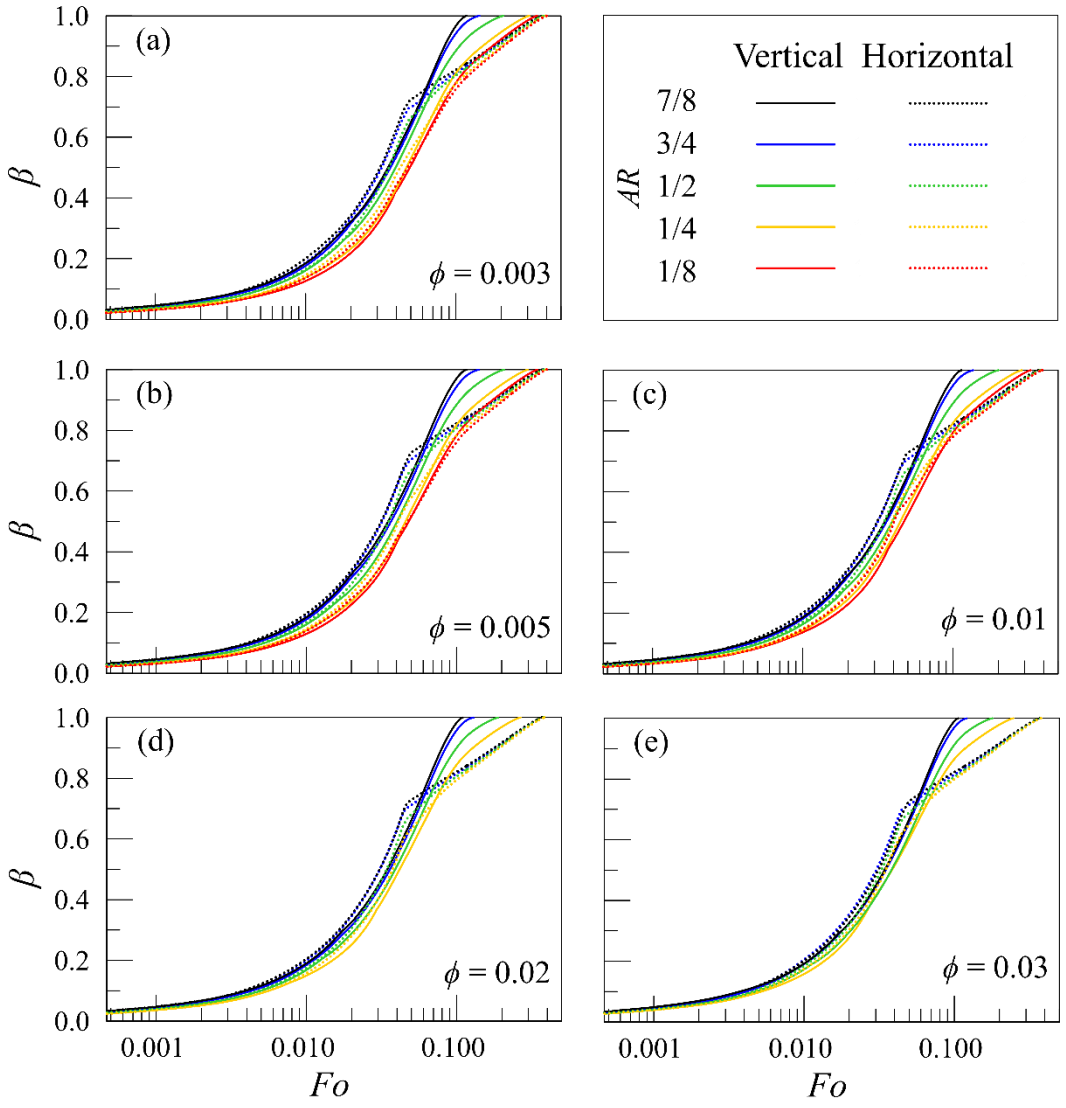

581

582 Figure 9 – Liquid fraction (β) vs. *Fo,* for vertical and horizontal fins, with *AR* = 7/8,
583 3/4, 1/2, 1/4, and 1/8 for ϕ: (a) 0.003, (b) 0.005, (c) 0.01, (d) 0.02, and (e) 0.03.

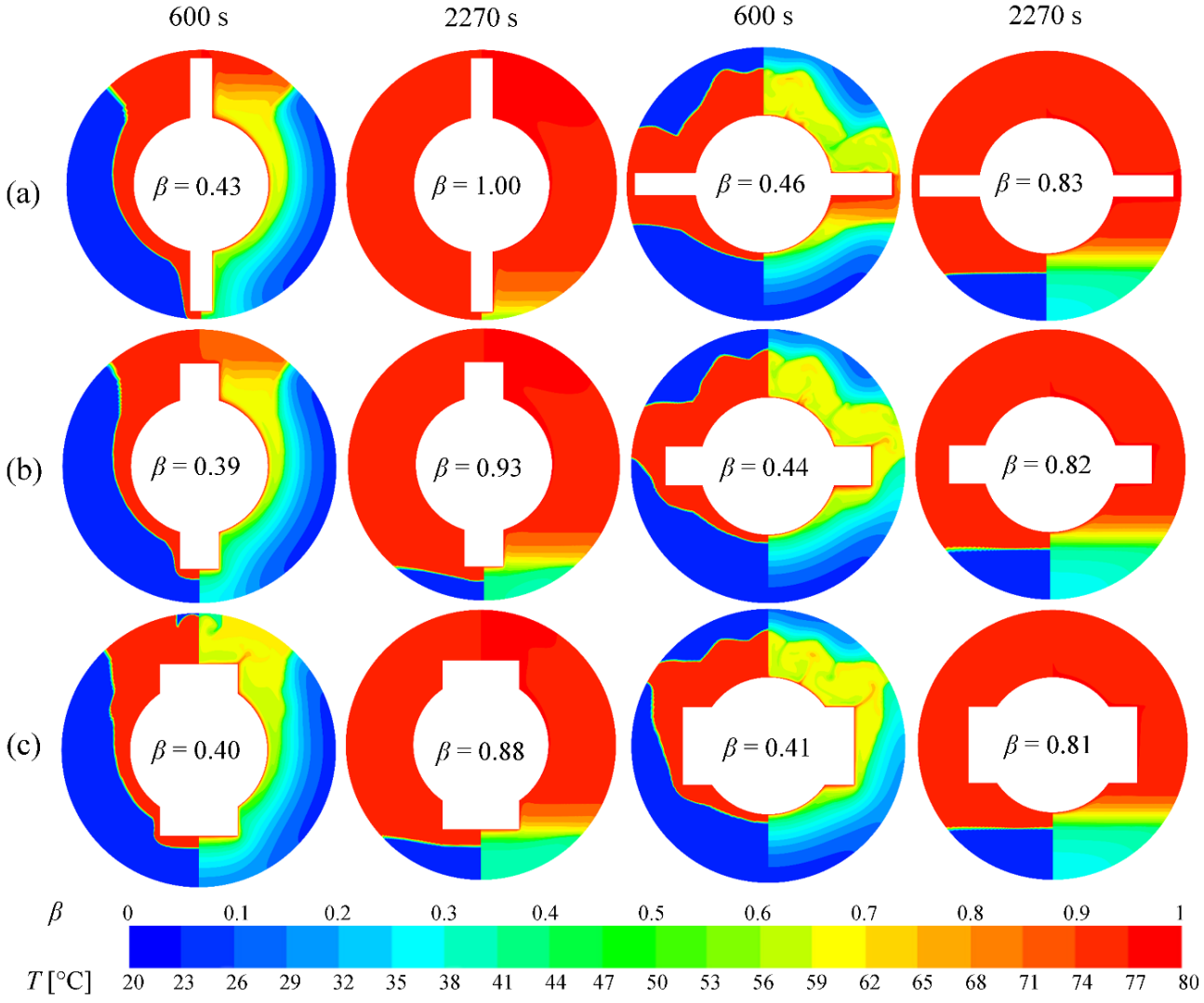

584

585 Figure 10 – Fields of β (left) and T (right), at t = 600 and 2,270 s, for vertical and
586 horizontal fins, with ϕ = 0.03 and AR: (a) 7/8, (b) 1/2, and (c) 1/4.

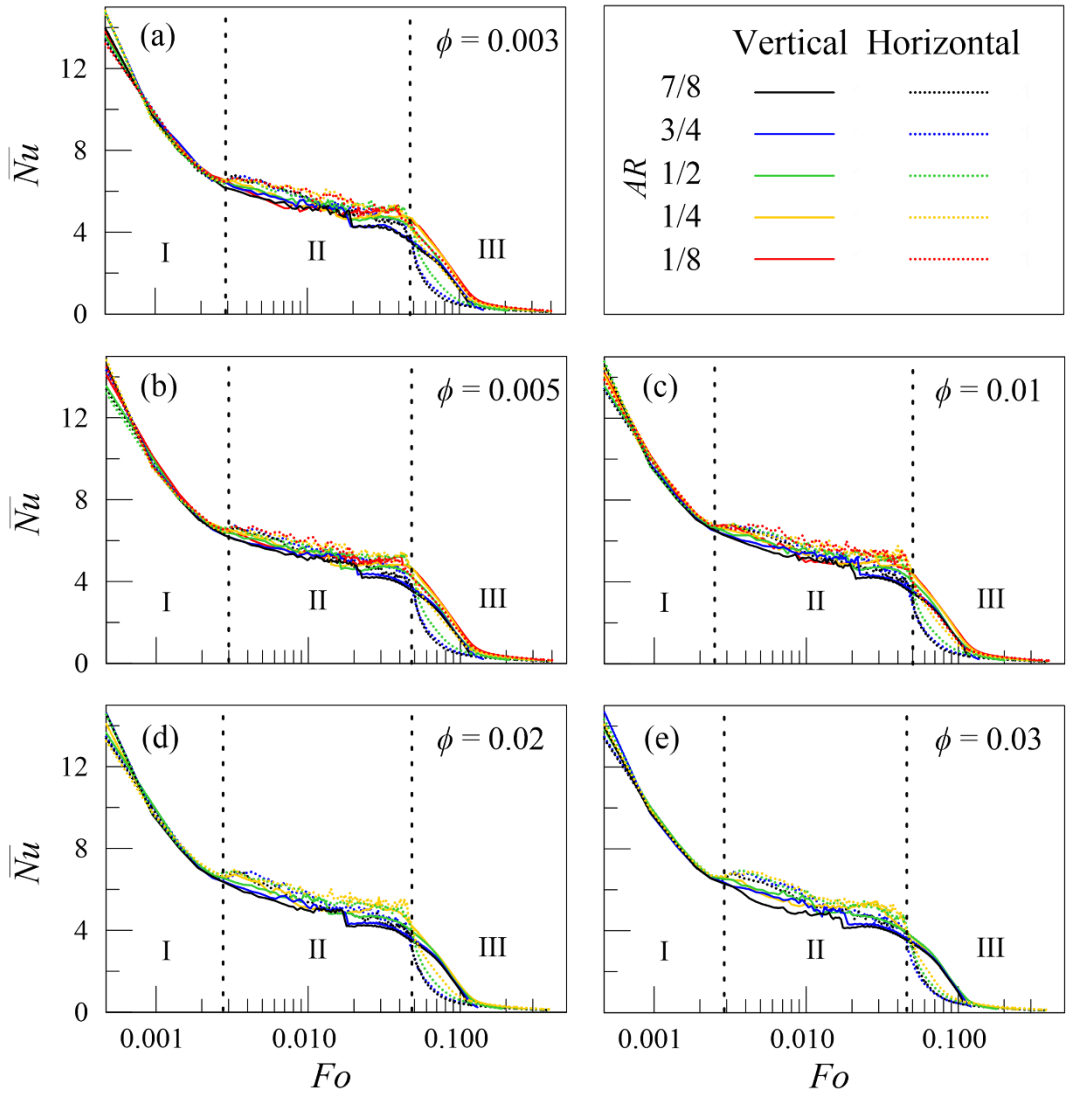

587

588 Figure 4 – $\overline{Nu}$ vs. *Fo* for vertical and horizontal fins, with *AR* = 7/8, 3/4, 1/2, 1/4, and
589 1/8 for ϕ: (a) 0.003, (b) 0.005, (c) 0.01, (d) 0.02, and (e) 0.03.

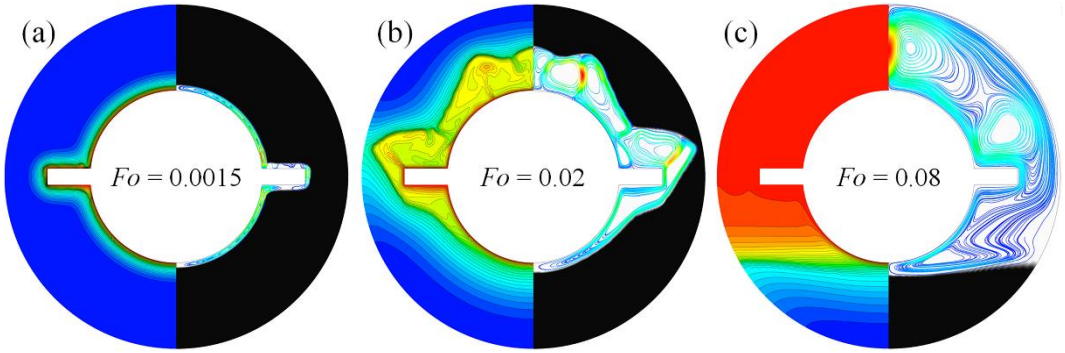

590

591 Figure 12 - Fields of *T* (left) and streamlines (right), for horizontal fins, with ϕ = 0.01,
592 and *AR* = 1/2, at *Fo*: (a) 0.0015, (b) 0.02, and (c) 0.08.

593

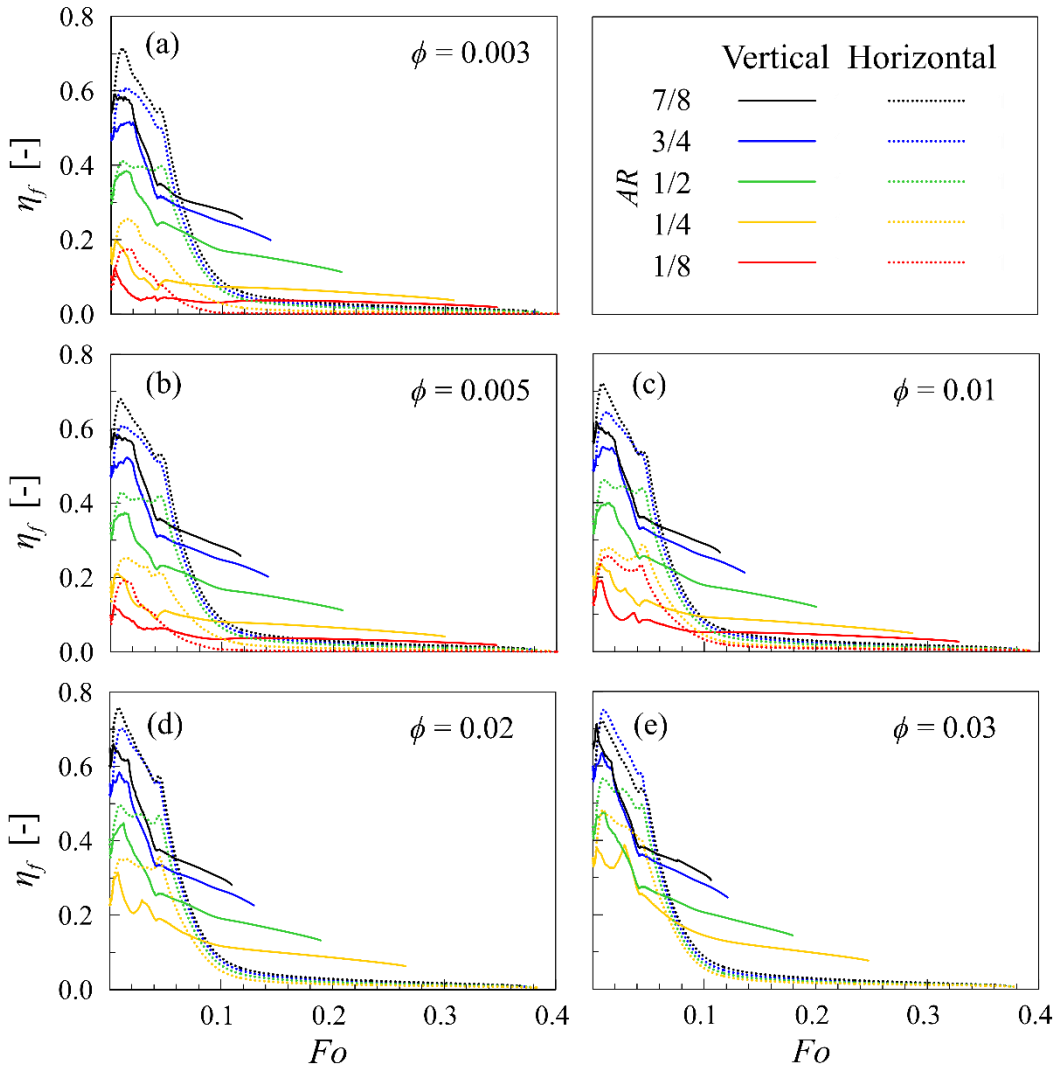

594 Figure 5 – Melting rate effectiveness (η_f) vs. *Fo*, for vertical and horizontal fins, with
595 *AR* = 7/8, 3/4, 1/2, 1/4, and 1/8 for ϕ: (a) 0.003, (b) 0.005, (c) 0.01, (d) 0.02, and
596 (e) 0.03.

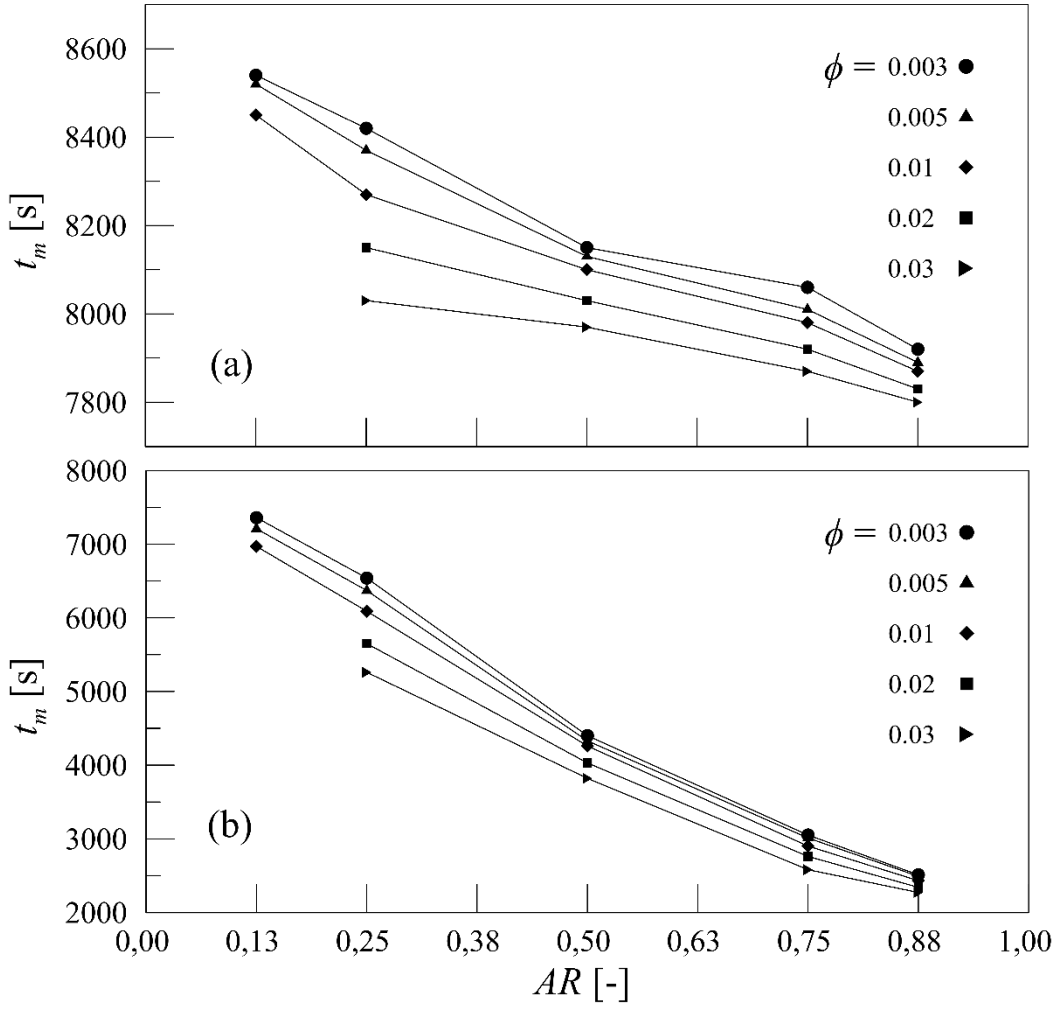

597 Figure 6 – Total melting time (t_m) vs. AR for ϕ = 0.003, 0.005, 0.01, 0.02, and 0.03*:*
598 (a) horizontal fins and (b) vertical fins.

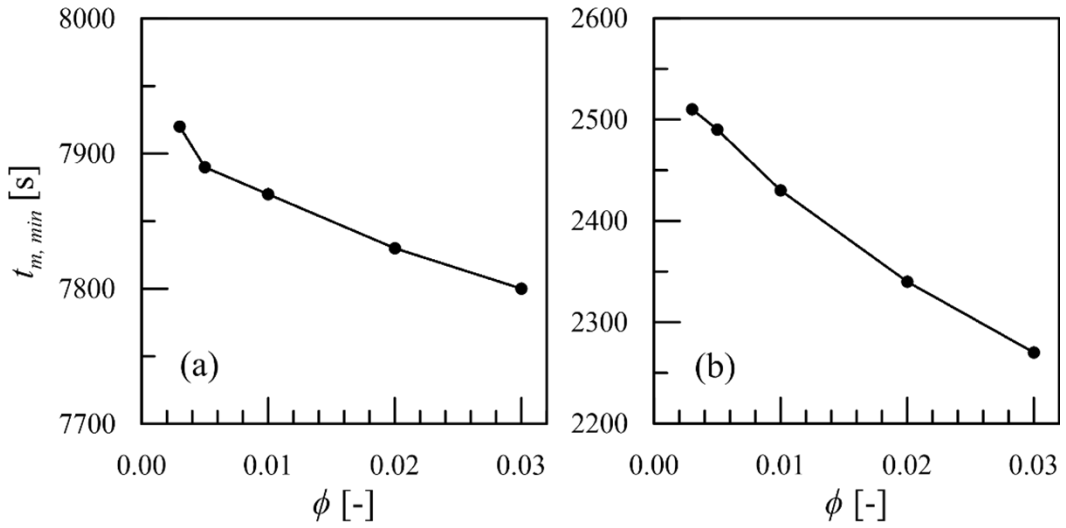

599 Figure 7 – Minimum total melting time ($t_{m,\,min}$) vs. ϕ for: (a) horizontal fins and
600 (b) vertical fins, both for AR = 0.88 (7/8).

601 Table 1 – Fin dimensions.

602

			AR				
			1/8	1/4	1/2	3/4	7/8
ϕ	0.003	e_f	4.00	2.00	1.00	0.67	0.57
		l_f	2.50	5.00	10.00	15.00	17.50
	0.005	e_f	7.54	3.77	1.88	1.26	1.08
		l_f	2.50	5.00	10.00	15.00	17.50
	0.01	e_f	15.08	7.54	3.77	2.51	2.15
		l_f	2.50	5.00	10.00	15.00	17.50
	0.02	e_f	30.16	15.08	7.54	5.03	4.31
		l_f	2.50	5.00	10.00	15.00	17.50
	0.03	e_f	45.24	22.62	11.31	7.54	6.46
		l_f	2.50	5.00	10.00	15.00	17.50

603 Table 2 – Thermophysical properties of lauric acid (Yuan et al. [23])

T_m [°C]	c_p [J kg^{-1} K^{-1}]	k [W m^{-1} K^{-1}]	Z [K^{-1}]	L [J kg^{-1}]	ρ [kg/m^3]	μ [kg m^{-1} s^{-1}]		
					60 °C	60 °C	70 °C	80 °C
44.2	2300	0.147	0.000615	173800	863	0.00534	0.00427	0.00347